View metadata, citation and similar papers at core.ac.uk

brought to you by CORE

provided by Queen Mary Research Online

On the early and developed stages of surface condensation: competition mechanism between interfacial and condensate bulk thermal resistances

Sun, J; WANG, HS

© The Author(s) 2016

This work is licensed under a Creative Commons Attribution 4.0 International License. The images or other third party material in this article are included in the article's Creative Commons license, unless indicated otherwise in the credit line; if the material is not included under the Creative Commons license, users will need to obtain permission from the license holder to reproduce the material. To view a copy of this license, visit http://creativecommons.org/licenses/by/4.0/

For additional information about this publication click this link.
http://qmro.qmul.ac.uk/xmlui/handle/123456789/15950

Information about this research object was correct at the time of download; we occasionally make corrections to records, please therefore check the published record when citing. For more information contact scholarlycommunications@qmul.ac.uk

On the early and developed stages of surface condensation: competition mechanism between interfacial and condensate bulk thermal resistances

Jie Sun[a*] and Hua Sheng Wang[b]

[a]*Institute of Engineering Thermophysics, Chinese Academy of Sciences, Beijing 100190, China*
[b]*School of Engineering and Materials Science, Queen Mary University of London, London E1 4NS, UK*

We use molecular dynamics simulation to investigate the early and developed stages of surface condensation. We find that the liquid-vapor and solid-liquid interfacial thermal resistances depend on the properties of solid and fluid, which are time-independent, while the condensate bulk thermal resistance depends on the condensate thickness, which is time-dependent. There exists intrinsic competition between the interfacial and condensate bulk thermal resistances in timeline and the resultant total thermal resistance determines the condensation intensity for a given vapor-solid temperature difference. We reveal the competition mechanism that the interfacial thermal resistance dominates at the onset of condensation and holds afterwards while the condensate bulk thermal resistance gradually takes over with condensate thickness growing. The weaker the solid-liquid bonding, the later the takeover occurs. This competition mechanism suggests that only when the condensate bulk thermal resistance is reduced after it takes over the domination can the condensation be effectively intensified. We propose a unified theoretical model for the thermal resistance analysis by making dropwise condensation equivalent to filmwise condensation. We further find that near a critical point (contact angle being ca. 153º) the bulk thermal resistance has the least opportunity to take over the domination while away from it the probability increases.

[*]Author to whom correspondence should be addressed. Electronic mail: sunjie@mail.etp.ac.cn (J Sun).

When a vapor is in contact with a solid surface at some temperature below the saturation temperature of the vapor, the vapor condenses to liquid on the surface, releasing to the surface the energy difference between the vapor and liquid states. The condensation mode is conventionally categorized as either dropwise or filmwise depending on the surface wettability. For a long time being, the general understanding of surface condensation has been acquired that dropwise condensation (DWC) and filmwise condensation (FWC) are two contrary modes and the former holds an order of magnitude more efficient in heat transfer than the latter [1,2]. The explanation has been given two-fold as: (1) the condensate bulk thermal resistance has been regarded as the crucial factor that determines the overall heat transfer performance and (2) the drop-shedding due to gravity makes DWC superior to FWC in reduction of condensate bulk thermal resistance. This understanding has been verified through plenty of experiments at conventional spatial and temporal scales. However, with the modern computer simulation methods [3-7], cutting-edge experimental resorts [8-13] and fast-developing nanomachining technologies [14-16], the microscopic, even molecular-level, phenomena, characteristics and dynamics become observable, manipulatable and customizable. It has been demonstrated that the surface wettability, essentially determined by the solid-fluid interaction, dominates various interfacial phenomena, e.g. velocity slip [6,7], temperature jump [6,7], liquid layering [11-13], contact angle [3,9,17] and droplet jumping [8,15,18]. When the surface condensation is re-investigated with the molecular-level insight, the conventional understanding has been challenged.

Our recent work [3], focused on the onset of surface condensation, has revealed the inherent connection between DWC and FWC through molecular dynamics simulation and classical nucleation theory. The solid-fluid interaction has been found as the origin to determine the surface condensation mode from the onset. A whole picture of condensation mode on surface with a wide range of wettability is given, where DWC is taken as the transition mode between no-condensation and FWC. In this work, we continue to explore the insight of surface condensation after the onset, i.e. the early and developed stages. We transform DWC equivalent to FWC in

terms of condensate bulk thermal resistance, enabling unified analysis of the complex phenomena. We reveal that the competition between the interfacial and condensate bulk thermal resistances determines the characteristics of time evolutions of different condensation modes and further the condensation intensities. The formation and transition mechanisms revealed in our previous work [3] presents the spatial characteristics of unification of surface condensation while the competition mechanism revealed in this work presents its temporal characteristics. These characteristics clarify a fundamental insight of the phenomenon of surface condensation.

Results

We use molecular dynamics (MD) simulation to characterize the early and developed stages of surface condensation. A long cuboid simulation box is chosen to take the general feature that affect both DWC and FWC at these stages and to eliminate the vapor-liquid-solid contact-line of DWC (see FIG. 1). The fluid-fluid interaction is governed by the Lennard-Jones (L-J) potential function. The fluid-solid interaction is also described by the L-J potential function, where the parameter β measures the relative strength of fluid-solid bonding. A small value of β means low surface free energy and hydrophobicity while a large value of β means higher surface free energy and hydrophilicity [6,7,19-23]. The surface wettability is commonly interpreted by contact angle θ, a readily measureable quantity [24-26]. To establish the correlation between β and θ, we primarily conduct MD simulations at thermal equilibrium states of $T = 0.75 \sim 0.85\ \varepsilon k_{\mathrm{B}}^{-1}$ (see FIG. 2), k_{B} being the Boltzmann constant. The result shows that θ decreases monotonically from 160^{o} to 20^{o} corresponding to β from 0.1 to 0.7.

We perform MD simulations for various values of fluid-solid bonding strength under non-isothermal conditions that the solid temperature varies in the range of $T_{\mathrm{s}} = 0.75 \sim 0.85\ \varepsilon k_{\mathrm{B}}^{-1}$ and the saturated vapor temperature is fixed at $T_{\mathrm{v}} = 1.0\ \varepsilon k_{\mathrm{B}}^{-1}$. The transient density profiles (see FIG. 3a) show that on the surface with $\beta = 0.1$, where the fluid-solid interaction is very weak, the condensate bulk can hardly form. On the contrary, the con-

densate bulk is seen to form readily on the surface with $\beta = 0.7$, where the fluid-solid interaction is very strong, and to keep growing thicker with time, indicating a high condensation intensity. Generally, the condensate bulk grows faster for higher β but the growth decreases with time. The transient temperature profiles (see FIG. 3b) show that with the condensate bulk forming on surface, a local temperature gradient establishes spontaneously within the condensate bulk connecting the solid-liquid and liquid-vapor interfaces. The range of the locally linear temperature profile widens with increasing thickness of the condensate bulk. During the widening, the local temperature at the solid-liquid interface gradually decreases approaching the surface temperature T_s while the local temperature at the liquid-vapor interface basically holds close to the vapor bulk temperature T_v. Note that the locally linear temperature profile fails to establish for $\beta = 0.1$ but behaves more regularly for higher β. Generally, the temperature gradient increases with increasing β but decreases with time. Both the density and temperature profiles suggest that the condensation intensity becomes higher with increasing β but lower with time.

As shown in FIG. 4, the condensation heat flux (q_c) originates from the vapor bulk distant from the condensing surface. With the vapor molecules approaching and condensing into the condensate bulk, the energy difference between the vapor and liquid states is released at the liquid-vapor interface. q_c then flows through the condensate bulk and across the solid-liquid interface via pure heat conduction (see linear temperature profile in FIG. 3b). Each step comes with a thermal resistance against q_c. Therefore, the overall thermal resistance (R_{total}) consists of the liquid-vapor interfacial thermal resistance (R_{lv}), the condensate bulk thermal resistance (R_l) and the solid-liquid interfacial thermal resistance (R_{sl}). Correspondingly, there are temperature drops from vapor to solid ΔT, namely, ΔT_{lv}, ΔT_l and ΔT_{sl}. Essentially, the characteristics of density and temperature profiles are closely related to the thermal resistances. The uniformity in both density and temperature profiles indicates the region of vapor bulk. The sudden drop in density profile corresponds to R_{lv}, the local linearity in

density and temperature profiles corresponds to R_{l} and the local temperature jump corresponds to R_{sl}. For a given vapor-to-solid temperature difference (ΔT), q_{c} is determined as:

$$q_{\mathrm{c}} = \frac{\Delta T}{R_{\mathrm{total}}} = \frac{\Delta T}{R_{\mathrm{lv}} + R_{\mathrm{l}} + R_{\mathrm{sl}}} \tag{1}$$

Since q_{c} holds through the thermal resistances, then we have

$$q_{\mathrm{c}} = \frac{\Delta T_{\mathrm{lv}}}{R_{\mathrm{lv}}} = \frac{\Delta T_{\mathrm{l}}}{R_{\mathrm{l}}} = \frac{\Delta T_{\mathrm{sl}}}{R_{\mathrm{sl}}} \tag{2}$$

In this work, ΔT is calculated as:

$$\Delta T = T_{\mathrm{v}} - T_{\mathrm{s}} \tag{3}$$

and q_{c} is calculated as:

$$q_{\mathrm{c}} = \left(h_{\mathrm{v}} - h_{\mathrm{l}}\right)\dot{n}_{\mathrm{c}} \tag{4}$$

where h_{v} and h_{l} are the specific enthalpies in vapor and condensate bulks, respectively (see details in [27]); $\dot{n}_{\mathrm{c}}$ is the condensed molecule flux, i.e. the time derivative of n_{c} (the number of condensed molecules per unit area). In the simulations, we carefully monitor the time evolution of n_{c} and find that n_{c} perfectly follows a second-order exponential increasing function, as:

$$n_{\mathrm{c}} = C_1 \exp(-\frac{t}{t_1}) + C_2 \exp(-\frac{t}{t_2}) + C_0 \tag{5}$$

where C_0, C_1, C_2 and t_1, t_2 are all coefficients. For demonstration, the time evolutions of n_{c} for the case of $T_{\mathrm{s}} = 0.75\ \varepsilon k_{\mathrm{B}}^{-1}$ and corresponding fitting curves are given in FIG. 5, from which we can clearly see that n_{c} grows decreasingly with time, fitting the second-order exponential increasing function, and increases with increasing β. $\dot{n}_{\mathrm{c}}$ is obtained by differentiation, as:

$$\dot{n}_{\mathrm{c}} = -\frac{C_1}{t_1}\exp(-\frac{t}{t_1}) - \frac{C_2}{t_2}\exp(-\frac{t}{t_2}) = C_1'\exp(-\frac{t}{t_1}) + C_2'\exp(-\frac{t}{t_2}) \tag{6}$$

where C_1' ($=-C_1/t_1$) and C_2' ($=-C_2/t_2$) are coefficients. Apparently, $\dot{n}_c$ follows a second-order exponential decreasing function. The time evolutions of n_c and $\dot{n}_c$ are shown in the first and second panels of FIG. 6, from which we find that, for a same β, the condensation intensity increases with increasing ΔT as expected.

The thickness of condensate bulk (δ) grows with condensation ongoing. For quantification, the liquid-side boundary of liquid-vapor interface is taken as the surface of the condensate bulk, which is the same as those in [28,29]. We have tried both the density-based method [30] and SRK equation-based method [28] to determine the surface position and find that the results agree well with each other. The time evolutions of δ are shown in the third panel of FIG. 6.

Since q_c can be calculated by Eq. (4) and ΔT_{lv}, ΔT_l and ΔT_{sl} can be determined directly from the temperature profiles (see FIG. 3b), consequently, R_{lv}, R_l and R_{sl} are readily obtained based on Eq. (2). With condensation ongoing, R_l apparently increases with increasing δ, as shown in the lowermost panel of FIG. 6. By correlating R_l and n_c to δ, we confirm $R_l \propto \delta \propto n_c$ through that all data of R_l and n_c fall well in linear functions of δ (see FIG. 7). It is implied that R_l and δ are also of the second-order exponential increasing functions of time as is n_c. On the other hand, R_{lv} is supposed to be solely dependent on the thermodynamic state of fluid and R_{sl} is known to be solely dependent on β. Therefore, for a given ΔT, the interfacial thermal resistances ($R_i = R_{sl} + R_{lv}$) essentially remain constant. In the simulations, R_{lv} is estimated to be $1.6\ \tau\sigma^{-2}k_B^{-1} \sim 3.8\ \tau\sigma^{-2}k_B^{-1}$ for $T_s = 0.75\ \varepsilon k_B^{-1}$ and $2.3\ \tau\sigma^{-2}k_B^{-1} \sim 5.1\ \tau\sigma^{-2}k_B^{-1}$ for $T_s = 0.85\ \varepsilon k_B^{-1}$ while R_{sl} is estimated to be $2.9\ \tau\sigma^{-2}k_B^{-1} \sim 12.8\ \tau\sigma^{-2}k_B^{-1}$ for $T_s = 0.75\ \varepsilon k_B^{-1}$ and $15.0\ \tau\sigma^{-2}k_B^{-1} \sim 38.2\ \tau\sigma^{-2}k_B^{-1}$ for $T_s = 0.85\ \varepsilon k_B^{-1}$. Clearly, R_{lv} is much smaller than R_{sl}. For demonstration, the time evolutions of R_i and R_l for $\beta = 0.3 \sim 0.7$ and $T_s = 0.75\ \varepsilon k_B^{-1}$ are shown in FIG. 8. We can clearly see the competition between R_i (the time-independent component) and R_l (the time-dependent component) over time. At the initial period of time, R_i undoubtedly dominates in R_{total} and holds while with condensation ongoing R_l gradually increases,

surpasses R_i and finally takes over the domination in R_{total}. Note that the condensation intensity is so low for $\beta = 0.1$ that R_i is not applicable and R_l keeps zero therefore these are not shown. By comparing FIG. 6 and FIG. 8, we find that the moments R_l surpassing R_i are basically the inflection points in the time evolutions of $\dot{n}_c$. Apparently, the initially fast decreasing part of $\dot{n}_c$ is dominated by R_i while the afterwards slow decreasing part is dominated by R_l. Since R_i is due to inherent properties of solid and fluid, which cannot be changed during condensation, while R_l is linearly correlated to δ, which is artificially removable during condensation, it is concluded that the condensation could be effectively intensified by removing R_l out of R_{total} only when R_l has defeated R_i. This provide clear guidance on how to enhance condensation heat transfer using highly-customized nano-machining and nano-coating surfaces [31-33].

Based on the above results that R_l grows as a second-order exponential increasing function of time while R_i is independent of time, we can finally achieve the following correlation from Eq. (1), as:

$$q_c = \frac{\Delta T}{R_i + R_l} \propto \frac{1}{1 - C_1'' \exp(-t/t_1) - C_2'' \exp(-t/t_2)} \tag{7}$$

where C_1'' and C_2'' are coefficients. This indicates that q_c is supposed to be an inversed second-order exponential decreasing function of time.

In addition, it is noteworthy that R_{sl} has been known to be correlated to β as a monotonically and non-linearly decreasing function [21,34,35]. Our estimation of R_{sl} agrees well with the published data and we further successfully fit all the data-points into an exponential decreasing function (see FIG. 9).

Discussion

The simulation system in this work can be used to directly analogize FWC with one-dimensional characteristics but not DWC, with inherent three-dimensional characteristics. To reasonably carry out a theoretical analysis of thermal resistance between FWC and DWC, we propose a unified model, where the condensate bulk

thermal resistance of DWC is made equivalent to that of FWC (see upper insert in FIG. 10a). For the conductive heat transfer through the condensate bulk with a temperature difference ΔT_l, the general equation has the form $\Delta T_\mathrm{l} = q_\mathrm{c} R_\mathrm{l}$. For FWC, $R_{\mathrm{l,FWC}} = \delta / \lambda$ therefore $\Delta T_\mathrm{l} = q_\mathrm{c} \delta / \lambda$ (λ being the thermal conductivity of condensate bulk and taken to be constant for simplification). For DWC, we normally have $\Delta T_\mathrm{l} = \bar{q}_\mathrm{c} \bar{R}_{\mathrm{l,DWC}} = Q_\mathrm{c} \bar{R}_{\mathrm{l,DWC}} / \bar{A}$, where Q_c, $\bar{q}_\mathrm{c}$, $\bar{R}_{\mathrm{l,DWC}}$ and $\bar{A}$ are the condensation heat transfer rate, equivalent condensation heat flux, equivalent condensate bulk thermal resistance and equivalent heat transfer area, respectively. Based on the ideally spherical crown for a single droplet on solid surface (see lower insert in FIG. 10a), the surfaces I and II are the isothermal surfaces and the distance ($\mathrm{d}\varepsilon$) between the two surfaces is the local thickness of the condensate bulk thermal resistance. The average value of $\mathrm{d}\varepsilon$ is obtained as:

$$\mathrm{d}\bar{\varepsilon} = \frac{d}{4\left(1+\cos\alpha\right)}\mathrm{d}\alpha \tag{8}$$

where d is the diameter of the contact circle. Therefore, $\bar{A}$ is calculated by the integral mean value of A, as:

$$\bar{A} = \frac{\int_0^{\bar{\varepsilon}_O} A\mathrm{d}\bar{\varepsilon}}{\int_0^{\bar{\varepsilon}_O} \mathrm{d}\bar{\varepsilon}} = \pi h^2 \left(\cot^2\frac{\theta}{2} + \frac{1}{3}\right) \tag{9}$$

where h is the height of the spherical crown. Note that $d = 2h\cot\frac{\theta}{2}$. On the other hand, for DWC, ΔT_l can be directly obtained by integrating the differential form of Fourier's equation of heat conduction, as

$$\Delta T_\mathrm{l} = \int_0^{\bar{\varepsilon}_O} \frac{Q_\mathrm{c}\mathrm{d}\bar{\varepsilon}}{\lambda A} = \frac{Q_\mathrm{c}\theta\tan\frac{\theta}{2}}{4\pi h\lambda} \tag{10}$$

We now have the expression for $\bar{R}_{\mathrm{l,DWC}}$ as

$$\bar{R}_{\mathrm{l,DWC}} = \frac{\Delta T_\mathrm{l}\bar{A}}{Q_\mathrm{c}} = \frac{h\theta\left(\cot\frac{\theta}{2} + \frac{1}{3}\right)}{4\lambda} \tag{11}$$

If we let $\bar{R}_{\mathrm{l,DWC}} = R_{\mathrm{l,FWC}}$, i.e. $\frac{\delta}{\lambda} = \frac{h\theta\left(\cot\frac{\theta}{2}+\frac{1}{3}\right)}{4\lambda}$, and we define an equivalent factor f $(=\delta/h)$, then we have

$$f = \frac{\theta}{4}\left(\cot\frac{\theta}{2}+\frac{1}{3}\right) \tag{12}$$

That means DWC with the height of h can be equivalently treated as FWC with the thickness of δ when Eq. (12) is satisfied. All the details of calculus are given in Supplementary Information. The curve of Eq. (12) is drawn in FIG. 10a. We find that the curve starts from $f = 0.5$ at $\theta = 0^\circ$ and then gradually increases with increasing θ (decreasing β) until it approaches around $\theta = 160^\circ$, after which it suddenly starts to grow increasingly towards infinity at $\theta = 180^\circ$. Note that $f = 1$ corresponds to $\theta \approx 150^\circ$. This variation indicates that (1) the condensate bulk thermal resistance of a droplet with $\theta = 0^\circ$ is equivalent to that of the condensate film with the thickness only half the height of the droplet ($f = 0.5$); (2) the condensate bulk thermal resistance of a droplet with $\theta = 180^\circ$ is equivalent to that of the condensate film with infinite thickness ($f \to \infty$); (3) the condensate bulk thermal resistance of a droplet with $\theta \approx 150^\circ$ is equivalent to that of the condensate film with the thickness being equal to the height of the droplet ($f = 1$); (4) the equivalent factor increases nonlinearly with increasing θ. Note that θ and β are not strictly linear to each other.

The curves of $\bar{R}_{\mathrm{l,DWC}}$, $R_{\mathrm{l,FWC}}$ and R_{i} (see FIG. 10b) show that $R_{\mathrm{l,FWC}}$ is solely dependent on δ while $\bar{R}_{\mathrm{l,DWC}}$ is dependent on both h and β. $\bar{R}_{\mathrm{l,DWC}}$ reduces decreasingly with increasing β and with an appreciable inflection point, which increases with increasing h. When h is small, e.g. $h = 100\ \sigma$, there is a range of $\bar{R}_{\mathrm{l,DWC}}$ below R_{i}, e.g. $\beta = 0.017 \sim 0.3$, meaning the latter overcomes the former. This range shrinks with increasing h. When h is large enough, e.g. $h \geq 500\ \sigma$, $\bar{R}_{\mathrm{l,DWC}}$ is no longer below R_{i} at any value of β, meaning the former takes the absolute domination regardless of condensate shape or condensation mode. The curves of R_{total} (see FIG. 10c) basically shape the same way as in FIG. 10b because R_{l} and R_{i} consti-

tute the overwhelming majority of R_{total}. Note that for FWC, R_{total} only includes R_{sl}, R_l and R_{lv}, while for DWC, a curvature-induced thermal resistance (R_{curv}) exists and is estimated as $R_{curv} = \Delta T_{curv} / q_c$, where ΔT_{curv} is calculated as [36]:

$$\Delta T_{curv} = \frac{r_{min}}{r} \Delta T \tag{13}$$

$$r_{min} = \frac{2T_{sat}\sigma_{st}}{h_{lv}\rho_l \Delta T} \tag{14}$$

where T_{sat} is the saturation temperature, σ_{st} is the surface tension at T_{sat}, h_{lv} is the latent heat and ρ_l is the condensate bulk density. In this work, r_{min} is estimated to be $r_{min} \approx 0.795\ \sigma$, which means that when $r > 10\ \sigma$ the relative influence of R_{curv} is less than 8%. Therefore, the effect of R_{curv} can be hardly felt in FIG. 10c. For proportional analysis, the curves of R_l / R_{total} ($R_l = \bar{R}_{l,DWC}$ for DWC and $R_l = R_{l,FWC}$ for FWC) are shown in FIG. 10d. We can clearly see that there exists a minimum for all curves corresponding to a common critical value of $\beta_{cr} \approx 0.105$ ($\theta_{cr} \approx 153^\circ$). This critical point actually corresponds to $f = 1$ in FIG. 10a with small deviation caused by R_{curv}. This means that for a given equivalent thickness to FWC, $f = 1$ guarantees the minimal R_l / R_{total}. The reason is two-sided: (1) When $\beta > \beta_{cr}$ ($\theta < \theta_{cr}$), $f < 1$ leads to decreasing R_l but R_{total} decreases due to more decreasing R_i (see FIG. 10a) therefore the resultant R_l / R_{total} increases; (2) When $\beta < \beta_{cr}$ ($\theta > \theta_{cr}$), $f > 1$ leads to more increasing R_l though R_{total} also increases due to increasing R_i (see FIG. 10a) therefore the resultant R_l / R_{total} also increases. This point could shed some light on the design and optimization of superhydrophobic surfaces for DWC, where the so-called self-propelled droplet-jumping (removal of R_l) takes place [15,37-39]. Based on the above-acquired second-order exponential correlation of R_l against time, we show the competition between R_l and R_i over time in FIG. 10e. We find that for FWC, R_l can easily defeats R_i with time lapse while for DWC, the probability decreases with decreasing β (increasing θ).

To clearly illustrate our competition mechanism, a schematic presentation is given in FIG. 11. We show the typical evolutions of R_l and R_i, corresponding to DWC with $\theta > 90^\circ$, DWC with $\theta < 90^\circ$ and FWC ($\theta = 0^\circ$), in the timeline. Generally, R_l grows decreasingly with time in a second-order exponential way while R_i generally keeps constant. We define the time when R_l surpasses R_i as the takeover time (t_{to}) and use it as the threshold between the early and developed stages. For DWC with $\theta > 90^\circ$, the solid-fluid interaction is very weak (small β) leading to large R_i. On the other hand, weak solid-fluid interaction hinders the mass and heat transfer hence weakens the condensation intensity leading to slowly increasing R_l. The resultant t_{to} is much delayed. For DWC with $\theta < 90^\circ$, the solid-fluid interaction is strong (large β) leading to small R_i. On the other hand, strong solid-fluid interaction enhances the mass and heat transfer hence strengthens the condensation intensity leading to quickly increasing R_l. The resultant t_{to} is advanced. For FWC, the solid-fluid interaction is very strong (larger β) leading to tiny R_i. On the other hand, very strong solid-fluid interaction significantly strengthens the condensation intensity leading to more quickly increasing R_l. The resultant t_{to} is extremely early. We find that the period of early stage is elongated with decreasing β. Note that β being extremely small ($\theta \to 180^\circ$) suggests infinite period of early stage. Since heat transfer with fixed temperature difference can be enhanced by reducing the thermal resistance, we emphasize that with fixed ΔT only in the developed stage the condensate is removed can the condensation be effectively enhanced. Otherwise, the heat transfer is still dominated by R_i and the removal is supposed to be in vain.

We point out that this work is more focused on the early stage of surface condensation when R_i is yet comparable to R_l. As shown in FIG. 10b, given sufficiently long time, R_l will defeat all the other thermal resistances and eventually become dominant in R_{total}. This is the developed stage of surface condensation, where the conventional understanding becomes applicable (see Introduction). We also point out that FIG. 11 provides us a whole picture of the transitional roles of thermal resistances for surface condensation. This work, in line

with our recent work on formation and transition mechanisms of condensation mode [3], further bridges the early stage to developed stage of surface condensation in terms of time evolutions of thermal resistances.

In summary, we use MD simulation to investigate the characteristics of condensate growth in the early and developed stages of surface condensation. We divide the thermal resistances into interfacial and condensate bulk components. The interfacial thermal resistances solely depend on the properties of solid and fluid, which are time-independent. However, the condensate bulk thermal resistance and also the condensate thickness and the number of condensed molecules, which are time-dependent, are all second-order exponential increasing functions of time. The condensation heat flux is supposed to be an inversed second-order exponential decreasing function of time. With condensation ongoing, there exists an inherent competition between the interfacial and condensate bulk thermal resistances and the resultant total thermal resistance determines the condensation intensity under a given vapor-solid temperature difference. The competition mechanism works as that the interfacial thermal resistance dominates at the onset of condensation and holds afterwards while the condensate bulk thermal resistance gradually takes over with condensate thickness growing. The takeover time is longer for a smaller β. This competition mechanism suggests that only when the condensate bulk thermal resistance is removed after it takes over the domination can the condensation be effectively intensified. Otherwise, the effectiveness could be little. To fairly carry out the thermal resistance analysis, we propose a unified theoretical model by making DWC equivalent to FWC. The theoretical results indicate that near the critical point ($\beta_{\mathrm{cr}} \approx 0.105$, $\theta_{\mathrm{cr}} \approx 153^{\circ}$), the condensate bulk thermal resistance has the least opportunity to take over the domination while away from it the probability increases. By implementing the correlation of condensate bulk thermal resistance with time, we find that for FWC the condensate bulk thermal resistance can easily defeats the interfacial thermal resistance over time while for DWC the probability decreases with increasing contact angle, i.e. decreasing β. We reveal the transitional roles of thermal resistances over time in surface condensa-

tions, which provides full understanding of the insight of the surface condensation for different modes over a whole range of conditions and bridges the early stage to developed stage of surface condensation.

Methods

The fluid-fluid interaction is governed by the Lennard-Jones (L-J) potential function, as:

$$\varphi(r) = 4\varepsilon\left[\left(\frac{\sigma}{r}\right)^{12} - \left(\frac{\sigma}{r}\right)^{6}\right] \tag{15}$$

where r is the intermolecular separation, σ and ε are the length and energy scales, respectively [40]. The function is truncated by the cut-off radius $r_c = 4.0\ \sigma$, beyond which the interactions are not considered. The fluid-solid interaction is also described by the L-J potential function with length scale $\sigma_{fs} = 0.91\ \sigma$ and energy scale $\varepsilon_{fs} = \beta\ \varepsilon$, where the parameter β measures the relative strength of fluid-solid bonding.

The solid wall, i.e. the condensing surface, is set at the bottom of the simulation box and represented by three layers of solid molecules forming a (111) plane of a face-centered cubic lattice with the lattice constant $\sigma_s = 0.814\ \sigma$. Neighboring solid molecules are connected by Hookean springs with the constant $k = 3249.1\ \varepsilon\sigma^{-2}$ [41]. Two extra layers of solid molecules are set below the three layers. The lower is stationary as a frame while the upper is governed by the Langevin thermostat, as:

$$\frac{\mathrm{d}\mathbf{p}_i}{\mathrm{d}t} = -\alpha\mathbf{p}_i + \mathbf{f}_i + \mathbf{F}_i \tag{16}$$

where $\mathbf{p}_i$ is the momentum of the *i*th solid molecule; $\alpha = 168.3\tau^{-1}$ is the damping constant [42], $\mathbf{f}_i$ is the sum of the forces acting on the *i*th solid molecule, $\mathbf{F}_i$ is a random force, of which each component is sampled from the Gaussian distribution with zero mean value and variance $2\alpha k_B T_s / \delta t$ ($\delta t = 0.002\ \tau$ is the time step, where $\tau = \sqrt{m\sigma^2/\varepsilon}$ is the time scale, m being the mass of a fluid molecule) [41,42]. The periodic boundary condition is applied at the sides and the diffuse reflection boundary is applied at the top end.

In each run, a relaxation period of $200\ \tau$ is used to keep the vapor saturated at $T = 1.0\ \varepsilon k_B^{-1}$, followed by

the condensation period of $60000\,\tau$ with the solid temperature at a value in the range of $T_s = 0.75 \sim 0.85\ \varepsilon k_B^{-1}$ and the saturated vapor temperature at $T_v = 1.0\ \varepsilon k_B^{-1}$, respectively. Extra vapor molecules are supplied through the upmost supply region (thickness $l_z/10$) by the USHER algorithm [43] immediately when the density within the supply region is lower than its initial saturation value. During the condensation period, the temperature in the supply region is controlled at $T_v = 1.0\ \varepsilon k_B^{-1}$ by the Langevin thermostat [20,44]. The surface wettability of solid wall changes from hydrophobicity to hydrophilicity by varying β from 0.1 to 0.7.

Acknowledgements

Financial supports from the National Natural Science Foundation of China (51406205), the Beijing Natural Science Foundation (3142021) and the Engineering and Physics Science Research Council (EPSRC) of the UK (EP/L001233/1) are acknowledged.

Author Contributions

J.S. developed the code, performed the simulations, prepared the manuscript, analyzed the results and reviewed the manuscript. H.S.W. analyzed the results and reviewed the manuscript.

Additional information

Competing financial interests: The authors declare no competing financial interests.

References

1 Rose, J. W. Dropwise condensation theory and experiment: a review. *Proceedings of the Institution of Mechanical Engineers, Part A: Journal of Power and Energy* **216**, 115-128 (2002).

2 Schmidt, E., Schurig, W. & Sellschopp, W. Versuche über die Kondensation von Wasserdampf in Film- und Tropfenform. *Forsch. Ing.* **1**, 53-63 (1930).

3 Sheng, Q., Sun, J., Wang, Q., Wang, W. & Wang, H.S. On the onset of surface condensation: Formation and transition mechanisms of condensation modes. *Sci Rep* **6**, 30764 (2016).

4 Cheng, Y. P., Xu, J. L. & Sui, Y. Numerical investigation of coalescence-induced droplet jumping on superhydrophobic surfaces for efficient dropwise condensation heat transfer. *Int J Heat Mass Tran* **95**, 506-516 (2016).

5 Nam, Y., Kim, H. & Shin, S. Energy and hydrodynamic analyses of coalescence-induced jumping droplets. *Appl Phys Lett* **103** (2013).

6 Sun, J., Wang, W. & Wang, H. S. Dependence between velocity slip and temperature jump in shear flows. *J Chem Phys* **138**, 234703 (2013).

7 Sun, J., Wang, W. & Wang, H. S. Dependence of nanoconfined liquid behavior on boundary and bulk factors. *Phys Rev E* **87**, 023020 (2013).

8 Narhe, R. D., Khandkar, M. D., Shelke, P. B., Limaye, A. V. & Beysens, D. A. Condensation-induced jumping water drops. *Phys Rev E* **80** (2009).

9 Chen, L., Yu, J. P. & Wang, H. Convex nanobending at a moving contact line: the missing mesoscopic link in dynamic wetting. *ACS Nano* **8**, 11493-11498 (2014).

10 Yu, J. P., Wang, H. & Liu, X. Direct measurement of macro contact angles through atomic force microscopy. *Int J Heat Mass Tran* **57**, 299-303 (2013).

11 Magnussen, O. M. *et al.* X-ray reflectivity measurements of surface layering in liquid mercury. *Phys Rev Lett* **74**, 4444-4447 (1995).

12 Regan, M. J. *et al.* Surface layering in liquid gallium - an X-ray reflectivity study. *Phys Rev Lett* **75**, 2498-2501 (1995).

13 Huisman, W. J. *et al.* Layering of a liquid metal in contact with a hard wall. *Nature* **390**, 379-381 (1997).

14 Li, X., Mao, L. & Ma, X. Dynamic behavior of water droplet impact on microtextured surfaces: the effect of geometrical parameters on anisotropic wetting and the maximum spreading diameter. *Langmuir* **29**, 1129-1138 (2013).

15 Miljkovic, N. *et al.* Jumping-droplet-enhanced condensation on scalable superhydrophobic nanostructured surfaces. *Nano Lett* **13**, 179-187 (2013).

16 Boreyko, J. B., Zhao, Y. & Chen, C.-H. Planar jumping-drop thermal diodes. *Appl Phys Lett* **99** (2011).

17 Niu, D. & Tang, G. H. The effect of surface wettability on water vapor condensation in nanoscale. *Sci Rep* **6**, 19192 (2016).

18 Enright, R. *et al.* How coalescing droplets jump. *ACS Nano* **8**, 10352-10362 (2014).

19 Thompson, P. A. & Robbins, M. O. Origin of stick-slip motion in boundary lubrication. *Science* **250**, 792-794 (1990).

20 Thompson, P. A. & Troian, S. M. A general boundary condition for liquid flow at solid surfaces. *Nature (London)* **389**, 360-362 (1997).

21 Xue, L., Keblinski, P., Phillpot, S. R., Choi, S. U. S. & Eastman, J. A. Two regimes of thermal resistance at a liquid-solid interface. *J Chem Phys* **118**, 337-339 (2003).

22 Dammer, S. M. & Lohse, D. Gas enrichment at liquid-wall interfaces. *Phys Rev Lett* **96** (2006).

23 Liu, C. & Li, Z. Molecular dynamics simulation of composite nanochannels as nanopumps driven by symmetric temperature gradients. *Phys Rev Lett* **105**, 174501 (2010).

24 Shirtcliffe, N. J., McHale, G., Atherton, S. & Newton, M. I. An introduction to superhydrophobicity. *Adv Colloid*

Interface **161**, 124-138 (2010).
25 Drelich, J., Chibowski, E., Meng, D. D. & Terpilowski, K. Hydrophilic and superhydrophilic surfaces and materials. *Soft Matter* **7**, 9804-9828 (2011).
26 Atefi, E., Mann, J. A. & Tavana, H. A robust polynomial fitting approach for contact angle measurements. *Langmuir* **29**, 5677-5688 (2013).
27 Sun, J., He, Y. L. & Tao, W. Q. Molecular dynamics-continuum hybrid simulation for condensation of gas flow in a microchannel. *Microfluid Nanofluid* **7**, 407-422 (2009).
28 Meland, R., Frezzotti, A., Ytrehus, T. & Hafskjold, B. Nonequilibrium molecular-dynamics simulation of net evaporation and net condensation, and evaluation of the gas-kinetic boundary condition at the interphase. *Phys Fluids* **16**, 223-243 (2004).
29 Meland, R. Molecular exchange and its influence on the condensation coefficient. *J Chem Phys* **117**, 7254-7258 (2002).
30 Wang, Z. J., Chen, M. & Guo, Z. Y. A molecular study on the liquid-vapor interphase transport. *Microscale Therm Eng* **7**, 275-289 (2003).
31 Enright, R., Miljkovic, N., Alvarado, J. L., Kim, K. & Rose, J. W. Dropwise condensation on micro- and nanostructured surfaces. *Nanosc Microsc Therm* **18**, 223-250 (2014).
32 Rykaczewski, K. *et al.* Dropwise condensation of low surface tension fluids on omniphobic surfaces. *Sci Rep* **4** (2014).
33 Das, A. K., Kilty, H. P., Marto, P. J., Andeen, G. B. & Kumar, A. The use of an organic self-assembled monolayer coating to promote dropwise condensation of steam on horizontal tubes. *J Heat Trans-T ASME* **122**, 278-286 (2000).
34 Maruyama, S. & Kimura, T. A study on thermal resistance over a solid-liquid interface by the molecular dynamics method. *Therm Sci Eng* **7**, 63-68 (1999).
35 Wang, C. S., Chen, J. S., Shiomi, J. & Maruyama, S. A study on the thermal resistance over solid-liquid-vapor interfaces in a finite-space by a molecular dynamics method. *Int J Therm Sci* **46**, 1203-1210 (2007).
36 Le Fevre, E. J. & Rose, J. W. in *Proceedings of the 3rd International Heat Transfer Conference* Vol. 2 362-375 (AIChE, Chicago, USA, 1966).
37 Chen, C.-H. *et al.* Dropwise condensation on superhydrophobic surfaces with two-tier roughness. *Appl Phys Lett* **90** (2007).
38 Boreyko, J. B. & Chen, C.-H. Self-propelled dropwise condensate on superhydrophobic surfaces. *Phys Rev Lett* **103** (2009).
39 Boreyko, J. B. & Chen, C.-H. Self-propelled jumping drops on superhydrophobic surfaces. *Phys Fluids* **22** (2010).
40 Allen, M. P. & Tildesley, D. J. *Computer simulation of liquids*. (Clarendon Press, 1987).
41 Yi, P., Poulikakos, D., Walther, J. & Yadigaroglu, G. Molecular dynamics simulation of vaporization of an ultra-thin liquid argon layer on a surface. *Int J Heat Mass Tran* **45**, 2087-2100 (2002).
42 Maruyama, S. in *Advances in numerical heat transfer* Vol. 2 (eds W. J. Minkowycz & E. M. Sparrow) Ch. 6, 189-226 (Tayler & Francis, 2000).
43 Delgado-Buscalioni, R. & Coveney, P. V. USHER: an algorithm for particle insertion in dense fluids. *J Chem Phys* **119**, 978-987 (2003).
44 Thompson, P. A. & Robbins, M. O. Shear flow near solids: Expitaxial order and flow boundary conditions. *Phys Rev A* **41**, 6830-6837 (1990).

Supplementary Information

As shown in the lower insert in FIG. 10a, the average distance $\mathrm{d}\bar{\varepsilon}$ between the surfaces I and II can be obtained by dividing the volume of the shaded part *V* by the basal area *A*. The volume of the shaded part equals to the volume difference of the spherical crown V_{I} subtracted by the spherical crown V_{II}, as:

$$\mathrm{d}\bar{\varepsilon} = \frac{V}{A} = \frac{V_{\mathrm{I}} - V_{\mathrm{II}}}{A} \tag{A1}$$

According to geometry, we have

$$\begin{aligned} V_{\mathrm{I}} &= \frac{\pi}{3}\left(3r_{\mathrm{I}} - h_{\mathrm{I}}\right)h_{\mathrm{I}}^2 \\ &= \frac{\pi}{3}\left[3r - r_{\mathrm{I}}\left(1-\cos\alpha\right)\right]r_{\mathrm{I}}^2\left(1-\cos\alpha\right)^2 \\ &= \frac{\pi r_{\mathrm{I}}^3}{3}\left(2+\cos\alpha\right)\left(1-\cos\alpha\right)^2 \\ &= \frac{\pi d^3\left(2+\cos\alpha\right)\left(1-\cos\alpha\right)^2}{24\sin^3\alpha} \end{aligned} \tag{A2}$$

$$\begin{aligned} V_{\mathrm{II}} &= \frac{\pi}{3}\left(3r_{\mathrm{II}} - h_{\mathrm{II}}\right)h_{\mathrm{II}}^2 \\ &= \frac{\pi}{3}\left\{3r - r_{\mathrm{II}}\left[1-\cos\left(\alpha+\mathrm{d}\alpha\right)\right]\right\}r_{\mathrm{II}}^2\left[1-\cos\left(\alpha+\mathrm{d}\alpha\right)\right]^2 \\ &= \frac{\pi r_{\mathrm{II}}^3}{3}\left[2+\cos\left(\alpha+\mathrm{d}\alpha\right)\right]\left[1-\cos\left(\alpha+\mathrm{d}\alpha\right)\right]^2 \\ &= \frac{\pi d^3\left[2+\cos\left(\alpha+\mathrm{d}\alpha\right)\right]\left[1-\cos\left(\alpha+\mathrm{d}\alpha\right)\right]^2}{24\sin^3\left(\alpha+\mathrm{d}\alpha\right)} \end{aligned} \tag{A3}$$

$$\begin{aligned} A &= 2\pi r_{\mathrm{I}}^2\left(1-\cos\alpha\right) \\ &= \frac{\pi d^2\left(1-\cos\alpha\right)}{2\sin^2\alpha} \\ &= \frac{\pi d^2}{2\left(1+\cos\alpha\right)} \end{aligned} \tag{A4}$$

Note that $r_{\mathrm{I}} = \dfrac{d}{2\sin\alpha}$ and $r_{\mathrm{II}} = \dfrac{d}{2\sin\left(\alpha+\mathrm{d}\alpha\right)}$

Considering Eqs. (A1)~(A4), we have

$$
\begin{aligned}
\mathrm{d}\bar{\varepsilon} &= \frac{d\sin^2\alpha}{12(1-\cos\alpha)}\left\{\frac{\left[2+\cos(\alpha+\mathrm{d}\alpha)\right]\left[1-\cos(\alpha+\mathrm{d}\alpha)\right]^2}{\sin^3(\alpha+\mathrm{d}\alpha)}-\frac{(2+\cos\alpha)(1-\cos\alpha)^2}{\sin^3\alpha}\right\} \\
&= \frac{d\sin^2\alpha}{12(1-\cos\alpha)}\left[\frac{(2+\cos\alpha)(1-\cos\alpha)^2}{\sin^3\alpha}\right]'\mathrm{d}\alpha \\
&= \frac{d\sin^2\alpha}{12(1-\cos\alpha)}\frac{3(\cos\alpha-1)^2}{\sin^4\alpha}\mathrm{d}\alpha \\
&= \frac{d(1-\cos\alpha)}{4\sin^2\alpha}\mathrm{d}\alpha \\
&= \frac{d}{4(1+\cos\alpha)}\mathrm{d}\alpha
\end{aligned}
\tag{A5}
$$

Therefore, we have the following integrals based on Eqs. (A4) and (A5)

$$
\begin{aligned}
\int_0^{\bar{\varepsilon}_O} A\mathrm{d}\bar{\varepsilon} &= \int_0^{\theta}\frac{\pi d^2}{2(1+\cos\alpha)}\frac{d}{4(1+\cos\alpha)}\mathrm{d}\alpha \\
&= \frac{\pi d^3}{8}\int_0^{\theta}\frac{\mathrm{d}\alpha}{(1+\cos\alpha)^2} \\
&= \frac{\pi d^3}{16}\left(\tan\frac{\alpha}{2}+\frac{1}{3}\tan^3\frac{\alpha}{2}\right)\Bigg|_0^{\theta} \\
&= \frac{\pi d^3}{16}\left(\tan\frac{\theta}{2}+\frac{1}{3}\tan^3\frac{\theta}{2}\right) \\
&= \frac{\pi h^3}{2}\left(\cot^2\frac{\theta}{2}+\frac{1}{3}\right)
\end{aligned}
\tag{A6}
$$

$$
\begin{aligned}
\int_0^{\bar{\varepsilon}_O}\mathrm{d}\bar{\varepsilon} &= \int_0^{\theta}\frac{d}{4(1+\cos\alpha)}\mathrm{d}\alpha \\
&= \frac{d}{4}\int_0^{\theta}\frac{1}{(1+\cos\alpha)}\mathrm{d}\alpha \\
&= \frac{d}{4}\tan\frac{\alpha}{2}\Bigg|_0^{\theta} \\
&= \frac{d}{4}\tan\frac{\theta}{2} \\
&= \frac{h}{2}
\end{aligned}
\tag{A7}
$$

$$
\begin{aligned}
\Delta T_{\mathrm{I}} &= \int_0^{\bar{\varepsilon}_o} \frac{Q_{\mathrm{c}}\,\mathrm{d}\bar{\varepsilon}}{\lambda_{\mathrm{I}} A} \\
&= \frac{Q_{\mathrm{c}}}{\lambda_{\mathrm{I}}} \int_0^{\theta} \frac{2\left(1+\cos\alpha\right)}{\pi d^2} \frac{d}{4\left(1+\cos\alpha\right)} \mathrm{d}\alpha \\
&= \frac{Q_{\mathrm{c}}}{2\pi d \lambda_{\mathrm{I}}} \int_0^{\theta} 1 \mathrm{d}\alpha \\
&= \frac{Q_{\mathrm{c}}}{2\pi d \lambda_{\mathrm{I}}} \alpha \Big|_0^{\theta} \\
&= \frac{Q_{\mathrm{c}} \theta}{2\pi d \lambda_{\mathrm{I}}} \\
&= \frac{Q_{\mathrm{c}} \theta \tan\dfrac{\theta}{2}}{4\pi h \lambda_{\mathrm{I}}}
\end{aligned}
\tag{A8}
$$

Note that $d = 2r_{\mathrm{I}} \sin\theta = \dfrac{2h\sin\theta}{1-\cos\theta} = \dfrac{2h}{\tan\dfrac{\theta}{2}}$.

Figure Legends

FIG. 1. Schematic of simulation system for surface condensation. The simulation size measures $l_x \times l_y \times l_z = 10.6\ \sigma \times 11.3\ \sigma \times 459.6\ \sigma$. The saturated vapor (red) is at $T_v = 1.0\ \varepsilon k_B^{-1}$. The solid wall (blue) is at the bottom and is at $T_s = 0.75 \sim 0.85\ \varepsilon k_B^{-1}$. The periodic boundary condition is applied at the sides and the diffuse reflection boundary is applied at the top end. The vaper supply region (thickness $l_z/10$) is at the top. The surface wettability of solid wall changes from hydrophobicity to hydrophilicity by varying β from 0.1 to 0.7.

FIG. 2. Correlations of contact angle (θ) with fluid-solid bonding parameter (β). The simulation size measures $l_x \times l_y \times l_z = 246.5\ \sigma \times 8.5\ \sigma \times 122.8\ \sigma$. The simulations are carried out in thermodynamic equilibrium state at T=0.75 εk_B^{-1} and 0.85 εk_B^{-1} with $\beta = 0.10 \sim 0.70$. The inserts are for T=0.75 εk_B^{-1}.

FIG. 3. Variations of the profiles of (a) density and (b) temperature in *z*-direction at different times (t) in the condensation period ($T_s = 0.75\ \varepsilon k_B^{-1}$).

FIG. 4. Schematic presentation of interfacial and condensate bulk thermal resistances.

FIG. 5. Time evolutions of number of condensed molecules (n_c) in the condensation period ($T_s = 0.75\ \varepsilon k_B^{-1}$).

FIG. 6. Time evolutions of number of condensed molecules (n_c), condensation flux ($\dot{n}_c$), thickness of condensate (δ) and condensate bulk thermal resistance (R_l) in the condensation period.

FIG. 7. Correlations of condensate bulk thermal resistance (R_l) and number of condensed molecules (n_c) with thickness of condensate bulk (δ) in the condensation period.

FIG. 8. Time evolutions of interfacial thermal resistance (R_i) and condensate bulk thermal resistance (R_l) in the condensation period.

FIG. 9. Correlation of solid-liquid interfacial thermal resistances (R_{sl}) with fluid-solid bonding parame-

ter (β).

FIG. 10. Analytical results of surface condensation. (a) The equivalent ratio ($f = \delta / h$) against contact angle (θ); (b) Competition between interfacial thermal resistance (R_{i}) and condensate bulk thermal resistance (R_{l}) against fluid-solid bonding parameter (β) and θ ; (c) Total thermal resistance (R_{total}) against β and θ ; (d) Ratio of R_{l} to R_{total} against β and θ ; (e) Transient variations of R_{l} and R_{i} against β and θ ($T_{\mathrm{s}} = 0.75\ \varepsilon k_{\mathrm{B}}^{-1}$).

FIG. 11. Schematic presentation of the competition mechanism between the interfacial and condensate bulk thermal resistances.

Figures

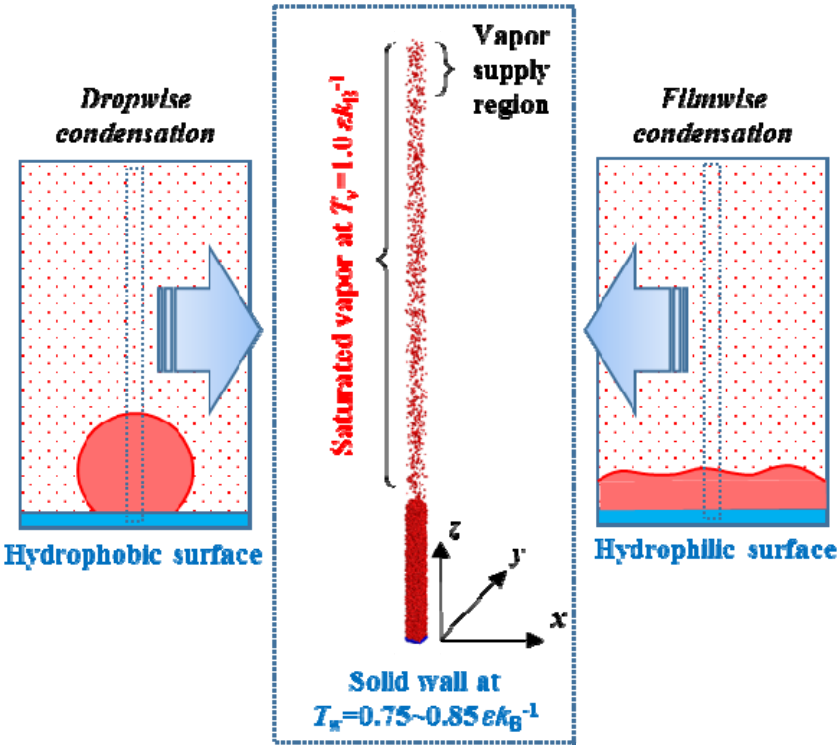

FIG. 1. Schematic of simulation system for surface condensation. The simulation size measures $l_x \times l_y \times l_z = 10.6\ \sigma \times 11.3\ \sigma \times 459.6\ \sigma$. The saturated vapor (red) is at $T_v = 1.0\ \varepsilon k_B^{-1}$. The solid wall (blue) is at the bottom and is at $T_s = 0.75 \sim 0.85\ \varepsilon k_B^{-1}$. The periodic boundary condition is applied at the sides and the diffuse reflection boundary is applied at the top end. The vaper supply region (thickness $l_z/10$) is at the top. The surface wettability of solid wall changes from hydrophobicity to hydrophilicity by varying β from 0.1 to 0.7.

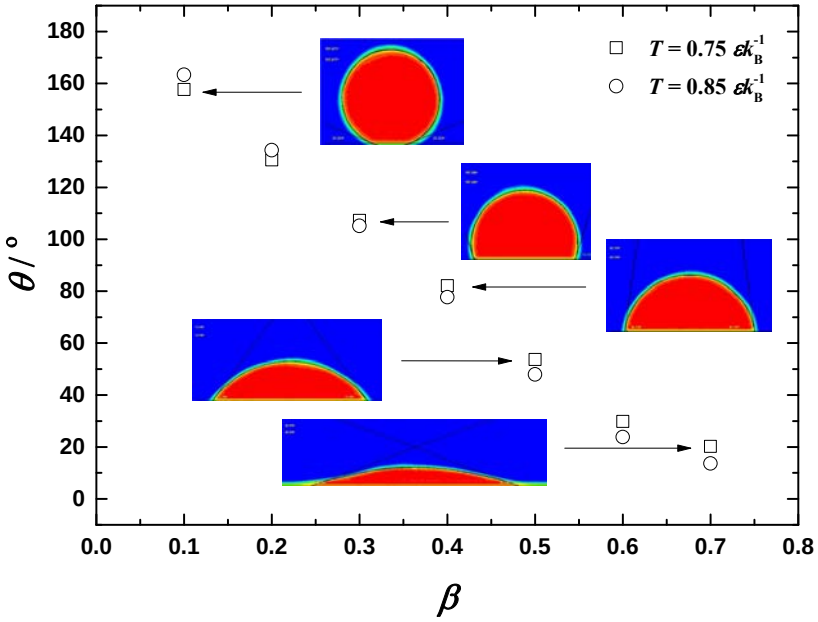

FIG. 2. Correlations of contact angle (θ) with fluid-solid bonding parameter (β). The simulation size measures $l_x \times l_y \times l_z = 246.5\ \sigma \times 8.5\ \sigma \times 122.8\ \sigma$. The simulations are carried out in thermodynamic equilibrium state at T=0.75 εk_B^{-1} and 0.85 εk_B^{-1} with $\beta = 0.10 \sim 0.70$. The inserts are for T=0.75 εk_B^{-1}.

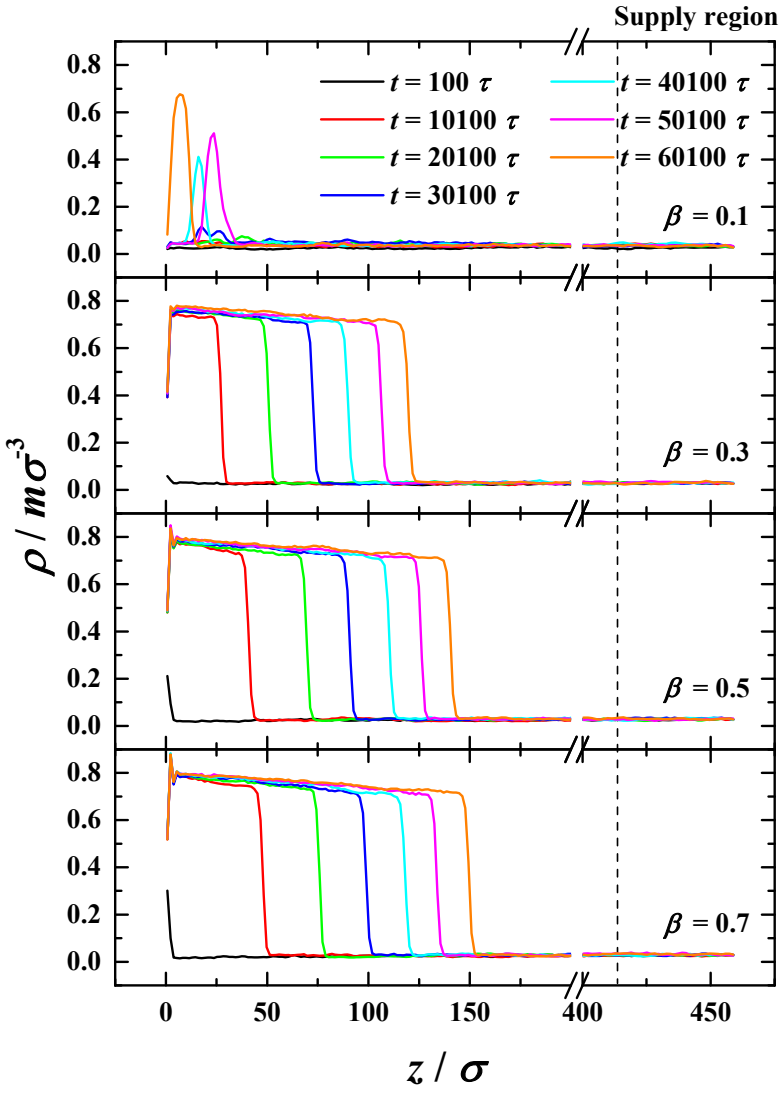
Supply region
t = 100 τ
t = 10100 τ
t = 20100 τ
t = 30100 τ
t = 40100 τ
t = 50100 τ
t = 60100 τ
β = 0.1
β = 0.3
β = 0.5
β = 0.7
ρ / mσ-3
z / σ
0.0
0.2
0.4
0.6
0.8
0
50
100
150
400
450

(a)

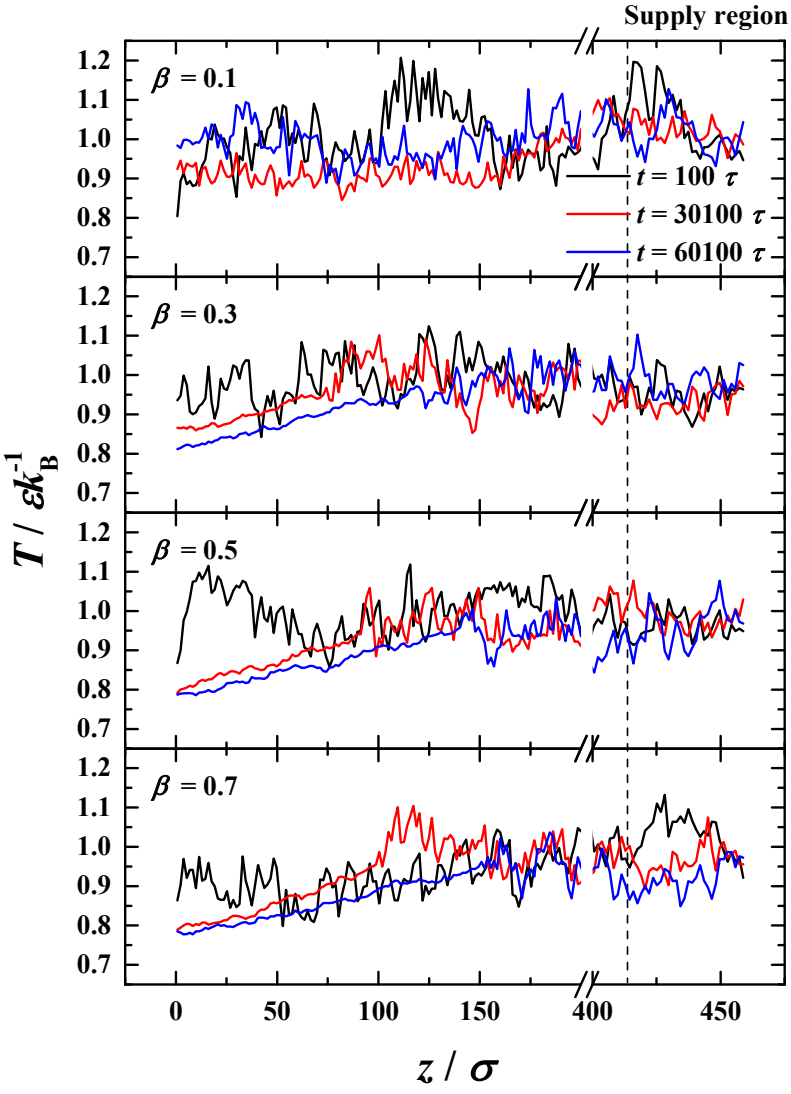

(b)

FIG. 3. Variations of the profiles of (a) density and (b) temperature in *z*-direction at different times (t) in the condensation period ($T_s = 0.75\ \varepsilon k_B^{-1}$).

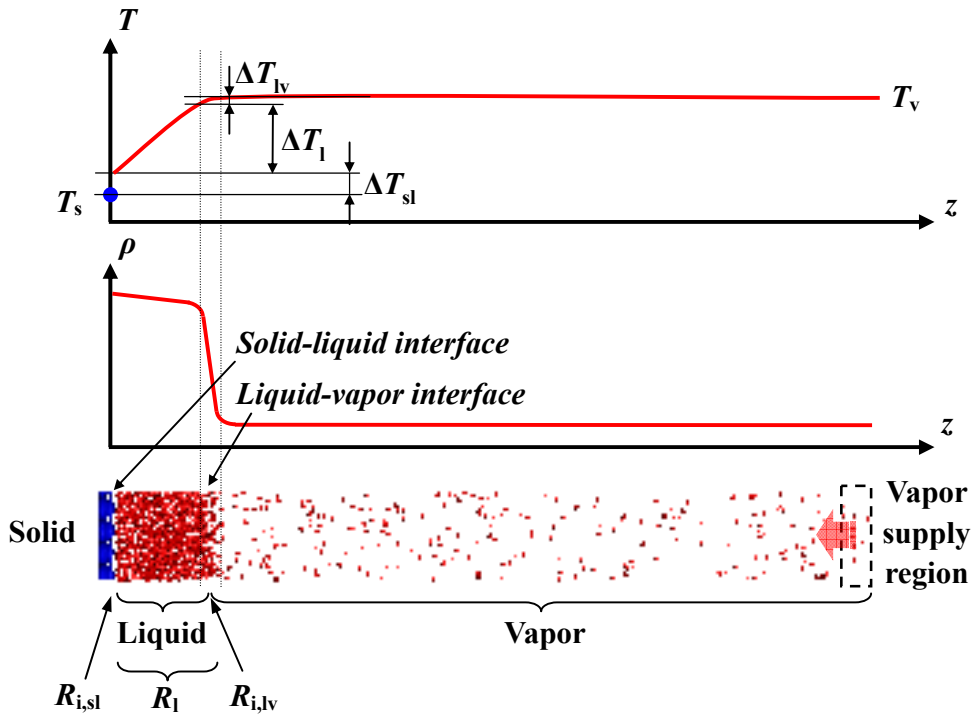

FIG. 4. Schematic presentation of interfacial and condensate bulk thermal resistances.

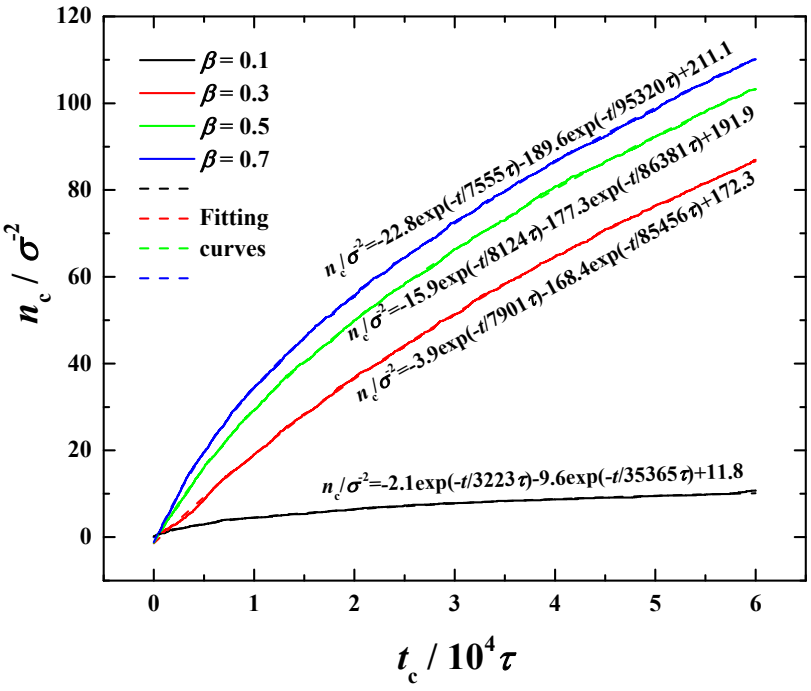

FIG. 5. Time evolutions of number of condensed molecules (n_c) in the condensation period ($T_s = 0.75\ \varepsilon k_B^{-1}$).

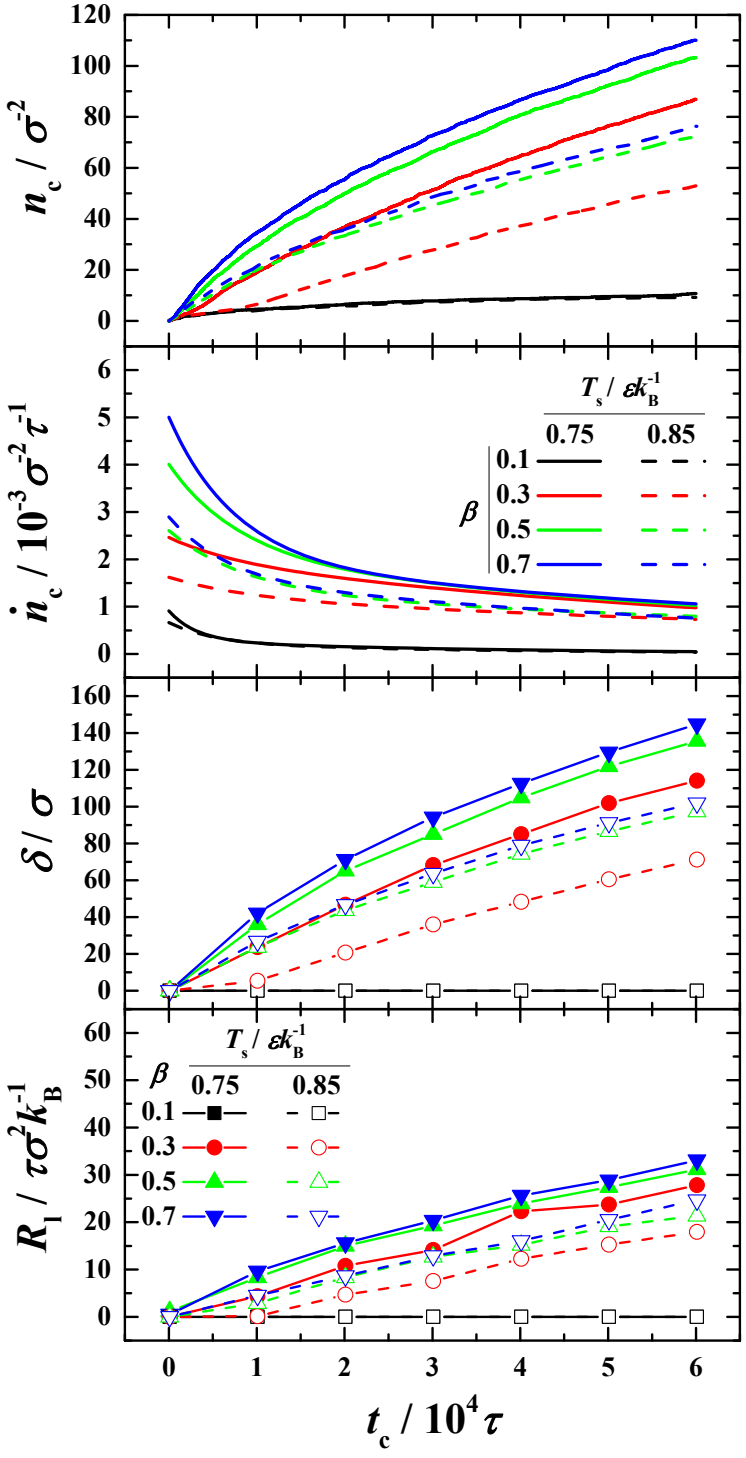

FIG. 6. Time evolutions of number of condensed molecules (n_c), condensation flux ($\dot{n}_c$), thickness of condensate (δ) and condensate bulk thermal resistance (R_l) in the condensation period.

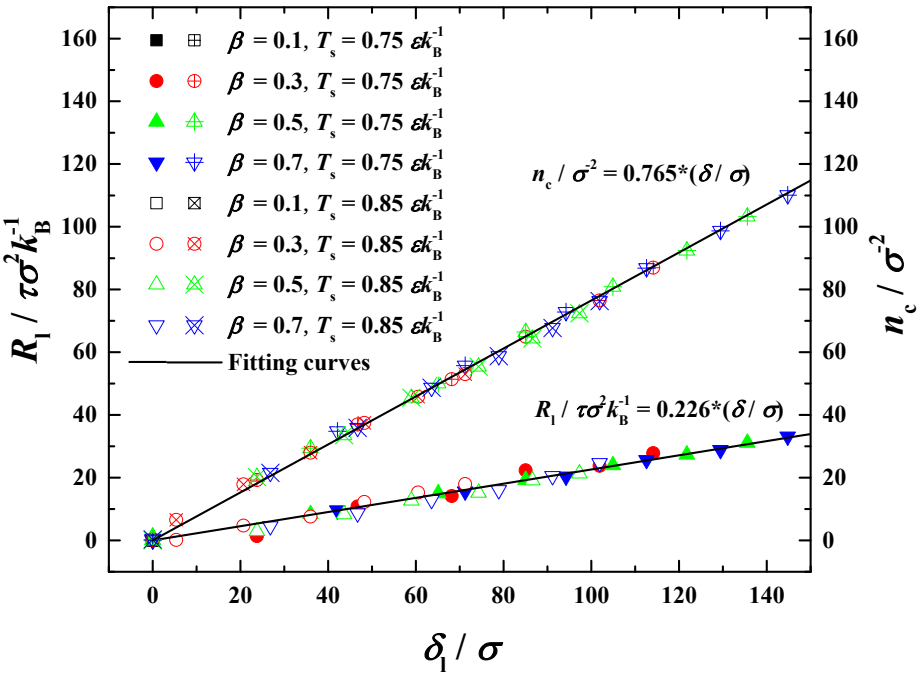

FIG. 7. Correlations of condensate bulk thermal resistance (R_l) and number of condensed molecules (n_c) with thickness of condensate bulk (δ) in the condensation period.

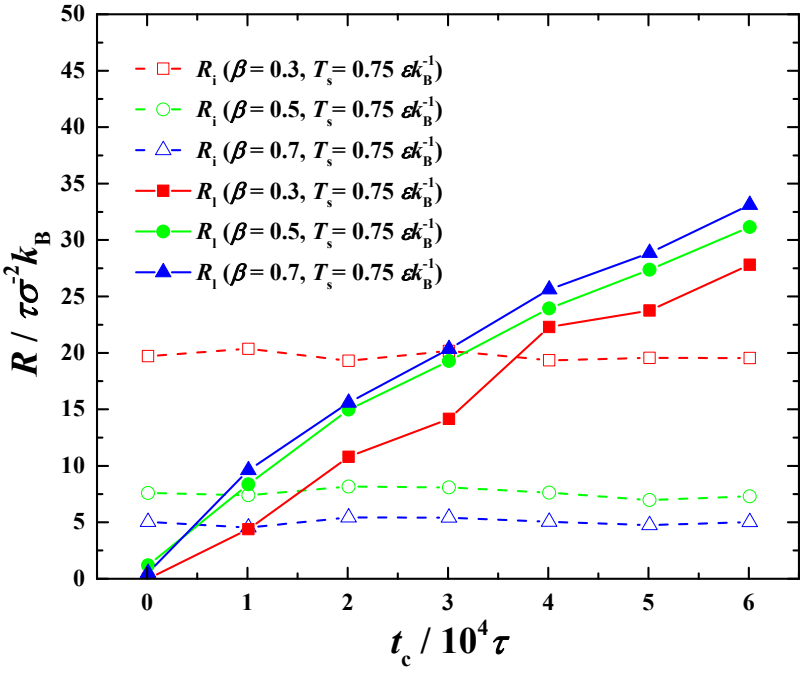

FIG. 8. Time evolutions of interfacial thermal resistance (R_i) and condensate bulk thermal resistance (R_l) in the condensation period.

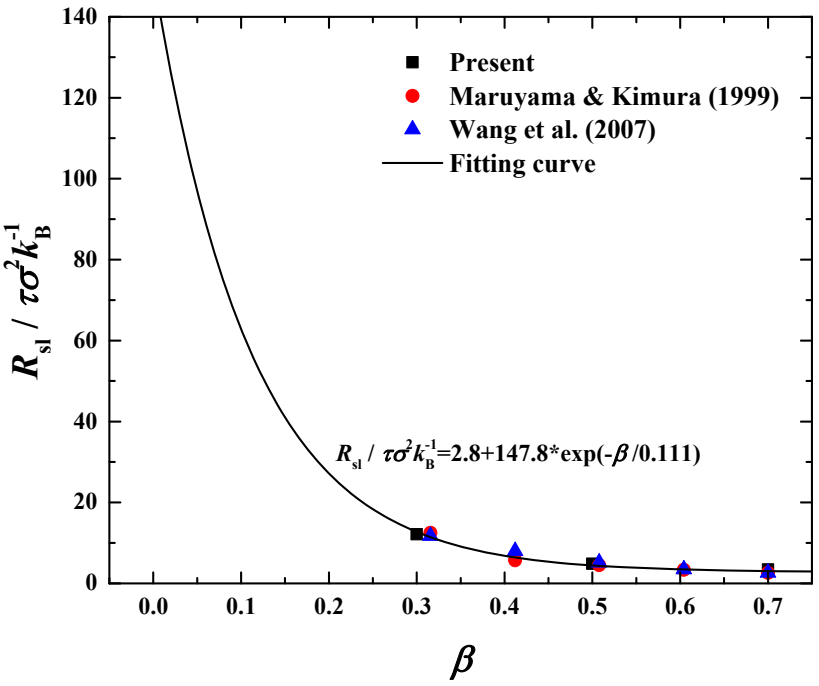

FIG. 9. Correlation of solid-liquid interfacial thermal resistances (R_{sl}) with fluid-solid bonding parameter (β).

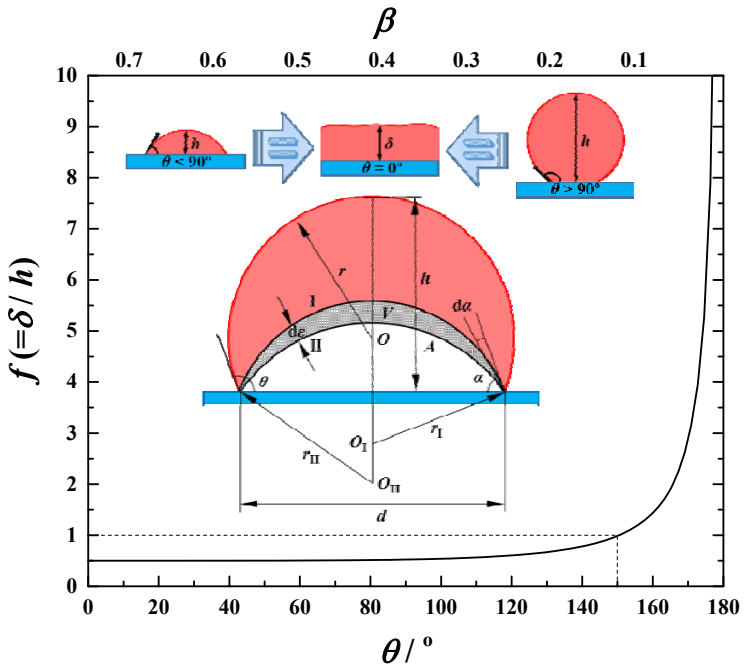
β
0.7 0.6 0.5 0.4 0.3 0.2 0.1
f (=δ / h)
θ / °
θ < 90°
θ = 0°
θ > 90°
h
δ
r
l
dβ
dθ
O
A
θ
α
O_I
O_II
r_I
r_II
d

(a)

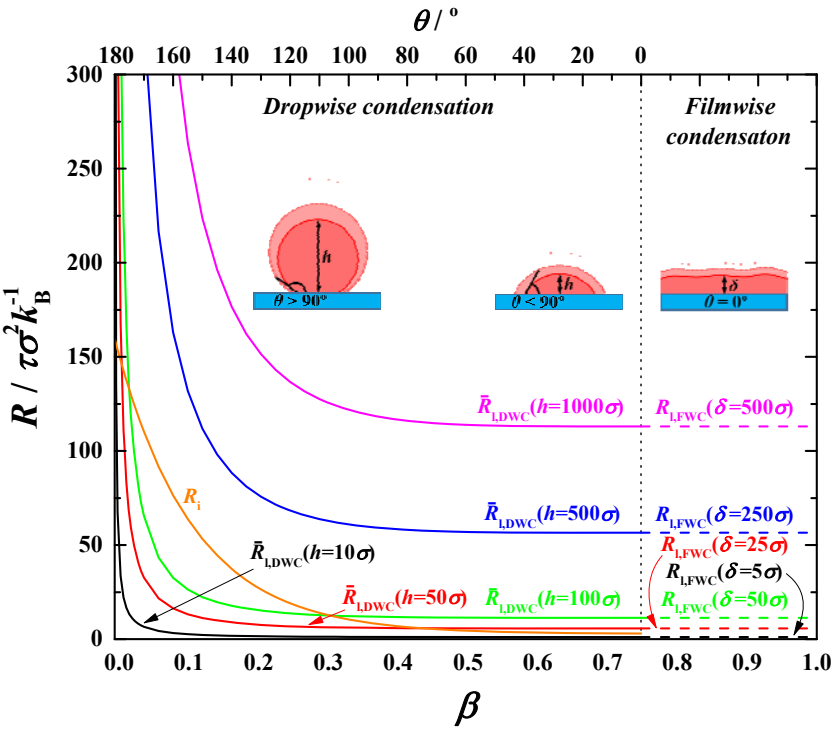
θ / °
180 160 140 120 100 80 60 40 20 0
R / τσ²k_B⁻¹
Dropwise condensation
Filmwise condensaton
θ > 90°
θ < 90°
θ = 0°
h
δ
R̄_I,DWC(h=1000σ)
R_I,FWC(δ=500σ)
R̄_I,DWC(h=500σ)
R_I,FWC(δ=250σ)
R_I,FWC(δ=25σ)
R_I,FWC(δ=5σ)
R_I,FWC(δ=50σ)
R_i
R̄_I,DWC(h=10σ)
R̄_I,DWC(h=50σ)
R̄_I,DWC(h=100σ)
β

(b)

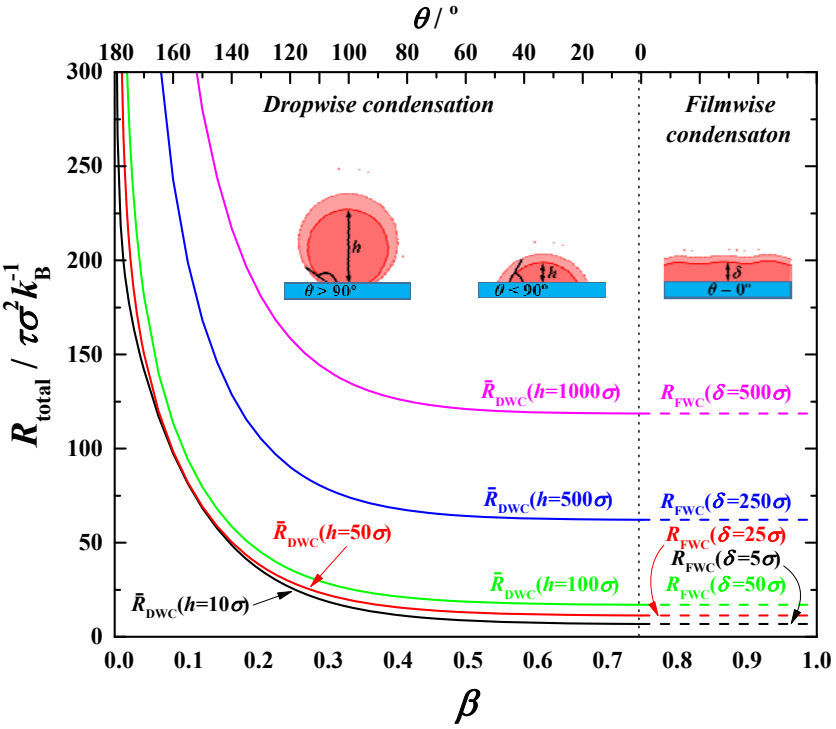
θ / °
180 160 140 120 100 80 60 40 20 0
Dropwise condensation
Filmwise condensaton
$R_{total} / \tau\sigma^2 k_B^{-1}$
$\bar{R}_{DWC}(h=1000\sigma)$
$R_{FWC}(\delta=500\sigma)$
$\bar{R}_{DWC}(h=500\sigma)$
$R_{FWC}(\delta=250\sigma)$
$\bar{R}_{DWC}(h=50\sigma)$
$R_{FWC}(\delta=25\sigma)$
$R_{FWC}(\delta=5\sigma)$
$\bar{R}_{DWC}(h=100\sigma)$
$R_{FWC}(\delta=50\sigma)$
$\bar{R}_{DWC}(h=10\sigma)$
θ > 90°
θ < 90°
θ = 0°
β

(c)

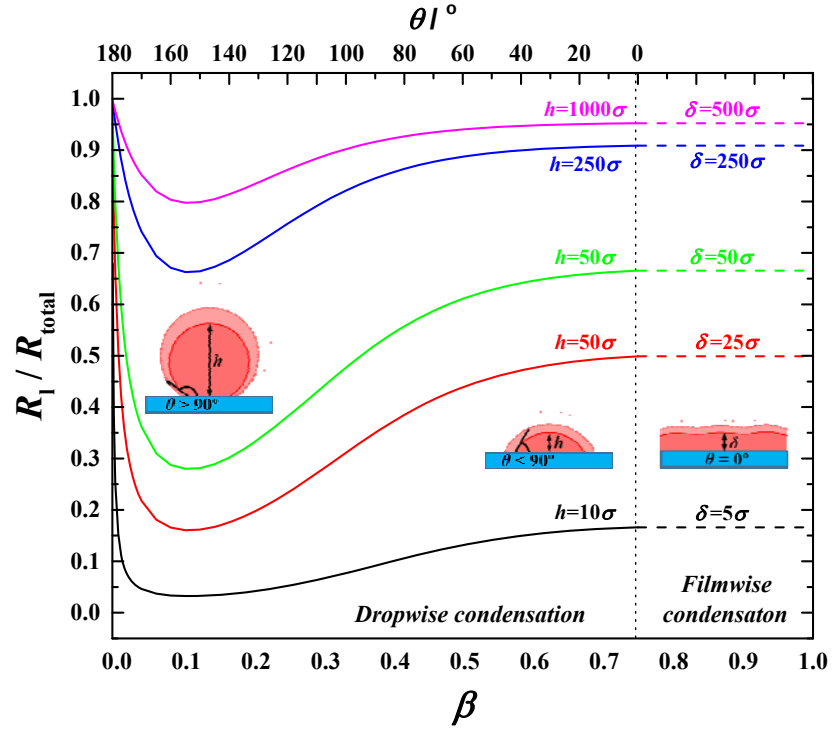
θ / °
180 160 140 120 100 80 60 40 20 0
R_1 / R_{total}
h=1000σ
δ=500σ
h=250σ
δ=250σ
h=50σ
δ=50σ
h=50σ
δ=25σ
h=10σ
δ=5σ
Dropwise condensation
Filmwise condensaton
θ > 90°
θ < 90°
θ = 0°
β

(d)

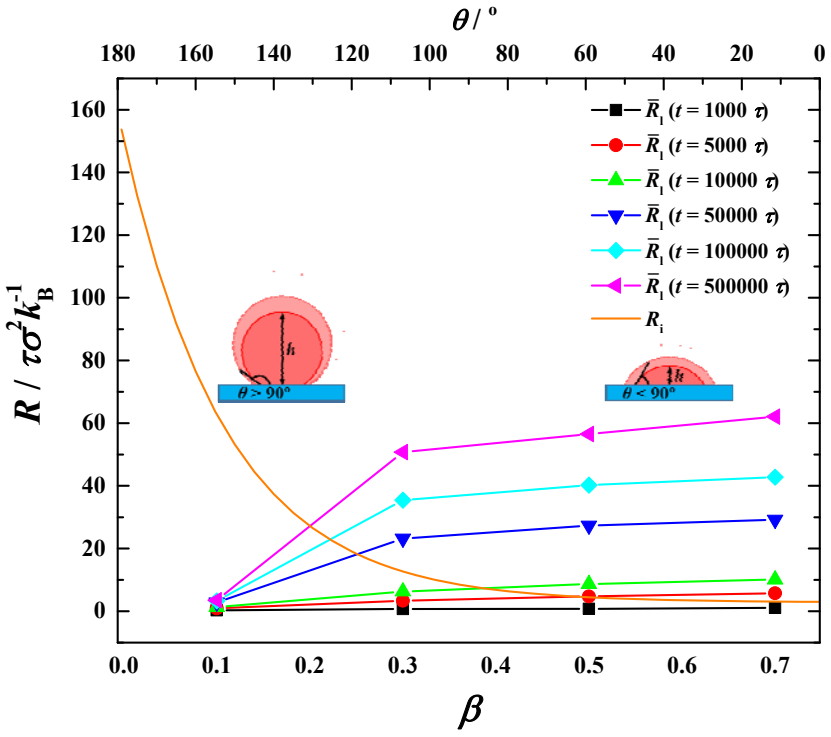

(e)

FIG. 10. Analytical results of surface condensation. (a) The equivalent ratio ($f = \delta / h$) against contact angle (θ); (b) Competition between interfacial thermal resistance (R_i) and condensate bulk thermal resistance (R_l) against fluid-solid bonding parameter (β) and θ; (c) Total thermal resistance (R_{total}) against β and θ; (d) Ratio of R_l to R_{total} against β and θ; (e) Transient variations of R_l and R_i against β and θ ($T_s = 0.75\ \varepsilon k_B^{-1}$).

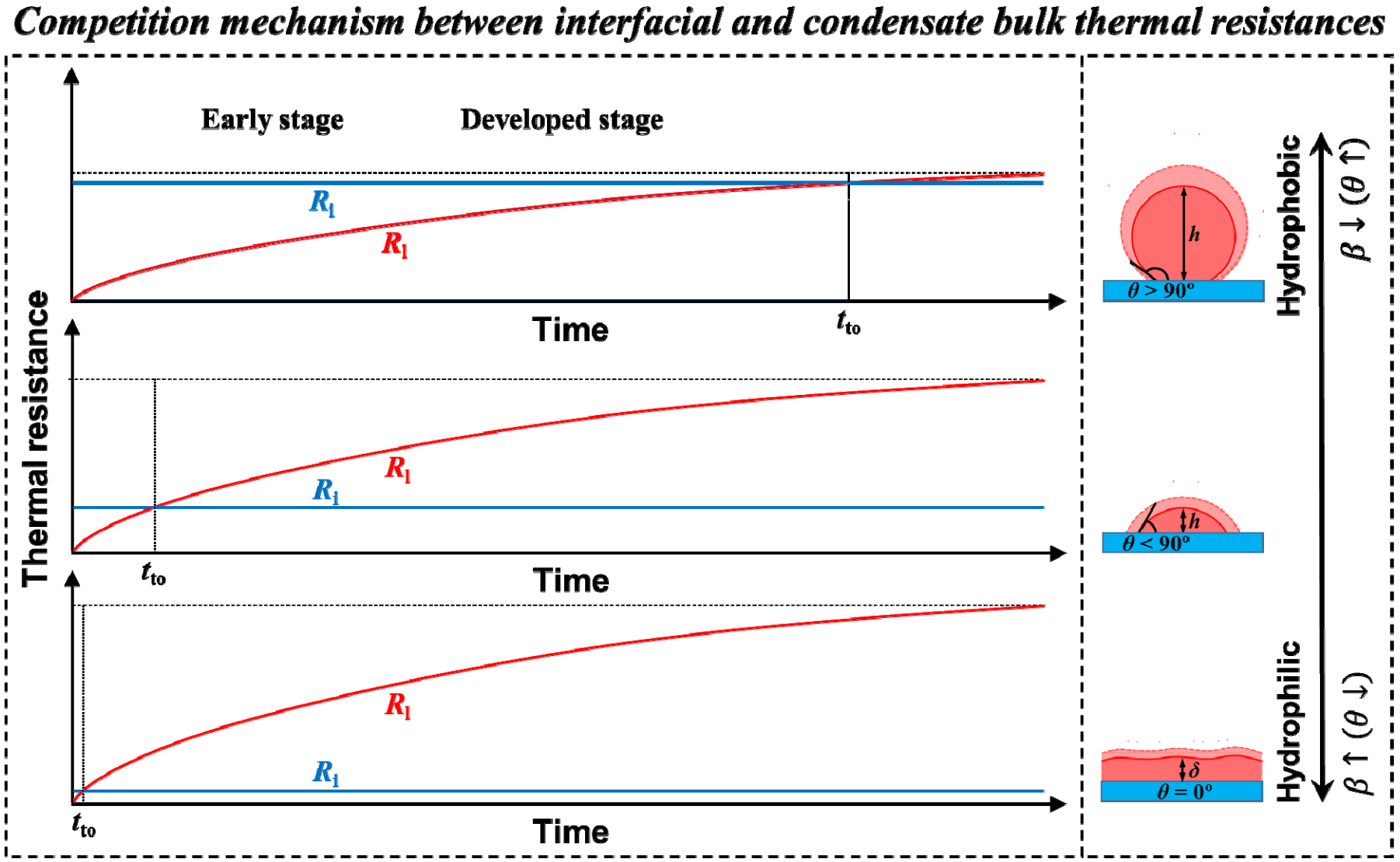

FIG. 11. Schematic presentation of the competition mechanism between the interfacial and condensate bulk thermal resistances.